This study focuses on the effects of N ions of different energies on PSi optical microcavities having an optimized ion fluence of 1E15 ions/cm^2. Three types of microcavities, namely, as-prepared (MC1), microcavities exposed with N ions with energies 200 keV (MC2), and 1MeV (MC3) having ion fluence of 1E15 ions/cm^2 were studied and compared. To understand the properties, various optical characterization techniques, namely optical reflectance, spatial-spectral mapping/imaging, Raman spectroscopy, and other techniques like X-ray photoelectron spectroscopy (XPS) and FE-SEM along with transfer matrix simulations were employed. The optical and structural properties of PSi based microcavities are appreciably modified by energetic nitrogen ions. These microcavities were characterized by various techniques, including reflection spectral mapping, FE-SEM, FTIR, Raman and XPS spectroscopy. The transfer matrix simulations are extensively used to analyze the experimental results. The optical features show significant modification after N ion-interaction produced a significant red-shift (~30-60 nm) of photonic cavity mode and colour changes in the microcavities. The higher energy (1 MeV) ions have enough energy to penetrate all the PSi layers and come to rest in bulk Si substrate. On the other hand, lower energy (200 keV) ions interact with the nanopores of the layers and settle down in the PSi layers leading to a modification of surface microstructure. In both MC2 and MC3 samples there is no direct damage or visible crack/crush is observed. The Raman results indicate that the Si- phase and Si-nanoparticle size can be tailored by varying the ion energy. The XPS study shows that bulk Si-Si bonds are replaced with bulk Si-N bonds during N ion implantation on the PSi microcavities surface. These ions collide with the Si atoms and lose their energy by breaking the Si-Si bonds and these broken bonds react with Nitrogen and generate Si–N bonds. The formation of Si_3-N_4 layers causes structural change, resulting in the variation in the PSi layers' porosities. This, in turn, would lead to an increase in the refractive index of PSi layers of the microcavities. The present work suggests that the ion beam technique could be potentially useful in the precise control over tunability of resonance cavity mode and controlled refractive index variation with careful optimization of ion penetration depth in PSi layers. These studies are further suitably utilized for the fabrication of various PSi photonic structure-based low-cost multi-dimensional optoelectronic devices such as PSi LEDs, tunable cavity mode LASERs, solar cells, tunable rugate, notch filters, omnidirectional mirrors, optical waveguides, detectors, sensors etc. [2]. Various ions **(H, He, Ar, N, O)** are used with the following ion irradiation parameters:

S. No.	Ion species	Energies (keV & MeV)	Ion-fluences (ions/cm^2)
1.	Ar	10 keV	1E14, 1E15, 5E15 & 1E16
2.	N	200 keV & 1MeV	1E15
3.	O	1MeV & 20 keV	1E13, 1E15, & 1E16
4.	He & H	35 keV	1E15, 5E15 & 1E16

REFERENCES:

[1] C. P. Verma, K. Asokan, P. K. Kanaujia, M. Adnan, D. Kanjilal, and G. Vijaya Prakash, Appl. Surf. Sci. **535**, 147696 (2021).

[2] C. P. Verma, M. Adnan, P. Srivastava, K. Asokan, D. Kanjilal, and G. Vijaya Prakash, J. Phys. D: Appl. Phys. **55**, 015104 (2022).

[3] C. P. Verma, K. Asokan, D. Kanjilal, and G. Vijaya Prakash, Mater. Lett. 306,130914 (2022).

5.2.28 Effect of Ar^{+6} ion irradiation on write-once-read many times memory behavior of am-BTO thin film

Amit Kumar Shringi[1], Mahesh Kumar[1]

[1]*Department of Electrical Engineering, Indian Institute of Technology Jodhpur, Jodhpur-342037, India.*

The rapid digitalization and extensive use of smart devices has raised the demand of more efficient and cost-effective memory systems. In such scenario when silicon-based memory system facing the issue of downscaling limit, the metal oxide based resistive switching devices seems to be most promising option for current memory requirement. Resistive switching devices has been investigated for different memory characteristics such write-once-read-many (WORM), dynamic random-access memory (DRAM) and flash memory. Among the all type of resistive switching characteristics, WORM device can be used for permanent archival of data is required such as RF identification tags. To study the resistive switching properties of amorphous $BaTiO_3$, we synthesized the $BaTiO_3$ powder by conventional solid state reaction method and prepared the sputtering target to deposit the $BaTiO_3$ thin film. $BaTiO_3$ thin film deposited on FTO coted substrate using RF-sputtering system at room temperature after achieving a base pressure of 7×10^{-7}m Bar. The chamber pressure was kept at 2×10^{-2}m Bar with argon flow of 50 SCCM and REF power of 50watt during deposition. We deposited the $BaTiO_3$ thin film for 120, 180 and 240nm

thickness by varying the deposition time to study the effect of thickness on resistive switching properties. After deposition we characterized the prepared thin films using AFM to study the surface morphology. Further we deposited silver top contact on prepared samples using thermal evaporation system with help of circular shadow mask of the diameter of 500µm. The prepared devices were electrically characterized using semiconductor parameter analyzer (Keithley 4200-SCS). The devices show the switching from a low-conductance state (LCS) to a high conductance state (HCS) by applying a low voltage signal (1.5 V). The device with 180 thickness shows the best on-off ratio on the order of 106 compared to 120 and 240 nm thick samples. The low on-off ratio and high current are caused by the pinholes in the surface of thin films in 120 and 240 nm samples. The fabricated devices exhibit long time date retention and good reading endurance. [1]

Further we irradiated our best performing 180nm thick $BaTiO_3$ thin film to study the effect of Ar^{+6} ion irradiation on write-once-read many times memory behavior. The $BaTiO_3$ thin films were deposited using RF-sputtering with the same parameter as discussed earlier. The prepared thin films were irradiated with Ar^{+6} ion in Low Energy Ion Beam Facility (LEIBF) at Inter University Accelerator Centre (IUAC), New Delhi. During the irradiation energy was fixed to 1.8MeV at three different ion fluence (1×10^{15} ions/cm^2, 3×10^{15} ions/cm^2 and 5×10^{15} ions/cm^2 with current of 1µA. Before placing the samples inside the chamber, we cleaned the target ladder and fixed the samples with the help of carbon tape. After placing the ladder, we evacuated the irradiation chamber to achieve high vacuum of the order of 10^{-6} mBar. Samples were perpendicularly placed to the beam line with help of positioner. The ion beam was focused to a spot of 10 mm diameter and then scanned over an area of 1×1 cm^2 using magnetic scanner to cover the complete sample surface for uniform irradiation. To investigate the morphological changes due to irradiation, the AFM images were recorded and analyzed and we observed a reduced roughness as a result of irradiation. Further the study of irradiation effect on WORM properties of $BaTiO_3$ thin films are under process.

REFERENCES:

[1] Amit Kumar Shringi, Atanu Betal, Satyajit Sahu, *and* Mahesh Kumar, "Write-once-read-many-times resistive switching behavior of amorphous barium titanate based device with very high on-off ratio and stability", Appl. Phys. Lett. **118**, 263505 (2021)

5.2.29 Growth and investigation of synergistic effect of TiO_2@CuCrS heterojunction for waste water treatment under solar energy

Vishnu Kutwade[1], and Ramphal Sharma[1]

[1]*Department of Physics, Dr. Babasaheb Ambedkar Marathwada University, Aurangabad-431004, India.*

In the perspective of low-cost, ecofriendly and stable photocatalyst for the waste water treatment, we have synthesized TiO_2@CuCrS nanocomposite via hydrothermal method. First, we have synthesized the TiO_2 nanoparticles via chemical precipitation technique. The CuCrS nanomaterial synthesized via hydrothermal method. To tailor the optical properties of CuS the transition metal chromium used as dopant. Synthesized TiO_2 nanoparticles were added into the CuCrS process and finally we get TiO_2@CuCrS nanocomposite. These nanomaterials CuCrS and TiO_2@CuCrS characterized via different techniques to explore their structural, optical and morphological properties. The structural study was carried out using D-8 Advanced diffractometer (Bruker AXS, Germany). The X-ray diffraction patterns of CuS nanoparticles and CuCrS thin film are depicted in Fig. 1 which confirms the hexagonal structures for both the samples compared with standard data card# 06-0464 [1]. As shown in Fig. 1 (a & b), the narrow sharp peaks of CuCrS thin film attribute the more crystallinity than the CuS. Fig. 1(c) shows the XRD pattern of anatase TiO_2 nanomaterials, and there are no other phase peaks observed. The optical properties and energy bandgap were recorded by (Perkin Elmer, LAMDA 25) Spectrophotometer in the wavelength range 300–1100 nm. The UV–visible absorption spectra of TiO2, CuS and CuCrS samples have been measured in the range of 200 to 1100 nm as shown in Fig. 2. From Taucs plot of Fig. 2(a, b, & c) the bandgap calculated values are 2.26 eV, 2.12 eV and 3.1 eV for CuS, CuCrS and TiO_2 nanoparticles, respectively. The chromium doping in CuS enhanced the optical absorption coefficient, and the red- shift in wavelength shows in Fig. 2 (a-b) concluded that the more number photons can be absorbed which enhanced the photosensing property of CuCrS nanomaterials. The transmission electron microscopy (TEM) analysis provides the morphological and elemental analysis of the prepared samples as shown in Fig. 3. Fig. 3a shows that the CuS has nanorod-like morphology. Fig. 3b shows the morphological image of the TiO_2@CuCrS nanomaterial. The composition of CuS and TiO2@CuCrS nanomaterial determined by EDS spectrum as shown in Fig. 4. The photocatalytic properties and activity analysis of prepared samples for before and after dye degradation are under process.

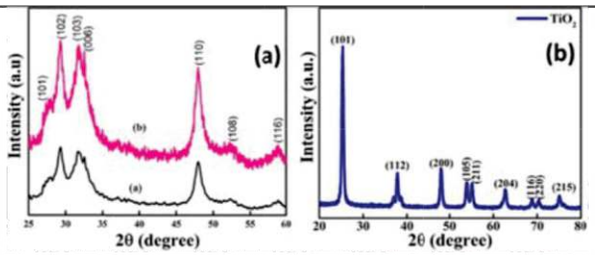

Fig. 1 XRD pattern of (a) CuS, (b) CuCrS, and (c) TiO_2 nanomaterials respectively.

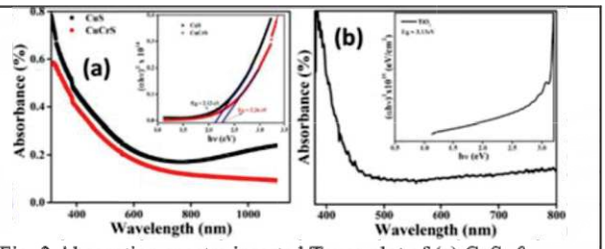

Fig. 2 Absorption spectra inserted Taucs plot of (a) CuS, & CuCrS, and (**b**) TiO_2 nanomaterials respectively.

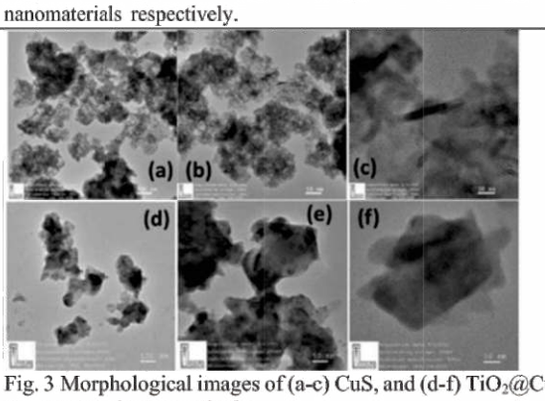

Fig. 3 Morphological images of (a-c) CuS, and (d-f) TiO_2@CuCrS nanocomposite respectively.

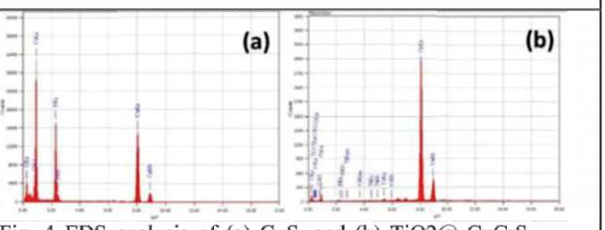

Fig. 4 EDS analysis of (a) CuS, and (b) TiO2@ CuCrS nanomaterials respectively.

REFERENCES:

[1] Deb, S. and P.K. Kalita, Journal of Materials Science: Materials in Electronics, **32**(19): p. 24125-24137(2021)

[2] Sun, Q., *et al*., New Journal of Chemistry, **44**(5): p. 1942-19525(2020)

5.2.30 Ion beam irradiation induced gold and silver nanomaterials as SERS substrate for chemical and biological sensing

Janavi Sirsul[1], Ambuj Tripathi[2], Dambarudhar Mohanta[3], Balaprasad Ankamwar[1]

[1]*Bio-inspired Materials Research Laboratory, Savitribai Phule Pune University (Formerly Pune University), Pune-411007 India.*
[2]*Materials Science Group, Inter-University Accelerator Centre (IUAC), Aruna Asaf Ali Marg, Vasant Kunj, New Delhi-110067, India.*
[3]*Department of Physics, Tezpur University, Napaam, Tezpur-784028, India.*

Nanomaterials majorly synthesized using physical, chemical and biological mode. Copper, gold and silver nanoparticles are SERS active substrates. Recently, we reported biosynthesis of 3D cross shaped copper micro/nano particles embedded on hexagonal base [1] and biosynthesis of star anise shaped copper micro/nano particles [2]. Herewith, we mainly focused on biosynthesis of gold and silver nanomaterials using plant leaves as a source of reducing and capping agents. The plant extract is abundance in nature, ecofriendly and economic. We reported first synthesis of triangular gold nanoprisms using lemon grass extract. Surfaces dependent activities of gold and silver nanoparticles play very important in catalytic, silver nanoparticles in SERS, gold and silver nanoparticles in bacteria detection. Here, we are reporting the biosynthesis of gold nanoparticles using novel source of plant extract as the source of reducing and capping agents. The synthesized gold nanoparticles were found to have desirable value of λ_{max} 555 nm with longitudinal peak at ~1100 nm.. UV-vis spectroscopy depicted primary signatures of gold nanoparticles. The morphological aspects of particles were revealed through Field Emission Scanning Electron Microscopy (FESEM). The particles were mixture of truncated hexagonal and spherical shapes. The crystalline nature of particles was studied through X-ray Diffraction (XRD). The particles had comparable 2θ values with the standard values present in JCPDS File No. 004-0784. 2θ values of synthesized particles are 38.12°, 44.32°, 64.6° and 77.54° correlating with planes (111), (200), (220) and (311) respectively. The probable biomolecules present in biological extract were identified by Nuclear Magnetic Resonance (NMR). Further studies on synthesis of silver nanoparticles and their use as SERS substrate in chemical and biological sensing and effect of beam line are currently in progress.

REFERENCES:

[1] U. Rahane, B. Chakraborty, A. Tripathi, D. Mohanta, B. Ankamwar, Poster Presentation, International E- Conference on Sustainable Development in Chemistry and Scientific Applications (ICSDCSA-2021), Organized by Department of Chemistry, Sadguru Gadage Maharaj College. Karad-415124, India. PP-13, p. 87, December 16-17(2021).

[2] B. Chakraborty, U. Rahane, A.Tripathi[2], D. Mohanta, B. Ankamwar Oral Presentation, International E-Conference on Sustainable Development in Chemistry and Scientific Applications (ICSDCSA-2021), Organized by Department of Chemistry, Sadguru Gadage Maharaj College. Karad-415124, India. OP-15, p.45, December 16-17(2021).

5.2.31 Study of 120 MeV Ag ion-induced effect on $Co_{0.5}Cu_{0.5}Fe_2O_4$/polypyrrole nanocomposites

Reena Dhyani*[1], R. C. Srivatava[1], Gagan Dixit[1], and R. C. Meena[2]

[1]*Govind Ballabh Pant University of Ag. & Technology, Uttarakhand, 243165, India*

[2]*Materials Science Division, Inter-University Accelerator Centre, New Delhi 110067, India*

Present work focuses on the study of 120 MeV Ag ion induced effects on $Co_{0.5}Cu_{0.5}Fe_2O_4$/polypyrrole (CCF- Ppy) nanocomposites. The nanocomposites of $Co_{0.5}Cu_{0.5}Fe_2O_4$–Ppy were synthesized by in-situ chemical polymerization method which consisted of 50 weight percentage of polypyrrole. The polymerization was carried out in the presence of already prepared $Co_{0.5}Cu_{0.5}Fe_2O_4$ nanoparticles. Synthesized samples were irradiated using 15 UD Pelletron accelerator at Inter University Accelerator Centre (IUAC), New Delhi with 120 MeV Ag^{9+} ions at different ion fluence i.e.1×10^{11}ions/cm^2,5×10^{11} ions/cm^2, 1×10^{12} ions/cm^2, 5×10^{12} ions/cm^2, and 1×10^{13} ions/cm^2, with current of 1pnA. The irradiated samples were characterized by XRD, Raman, VSM, and EPR characterization techniques. To study the effects on optical, and electrical properties of the irradiation the other measurements and analysis are under process.

Figure 1 depicts X-ray diffraction pattern of $Co_{0.5}Cu_{0.5}Fe_2O_4$/Ppy nanocomposites. It indicates that cubic crystal structure of composite does not get disturbed after irradiation, even at the highest fluence i.e. 1×10^{13} ions/cm^2. However, the width of XRD peaks increased and the intensities of peaks reduced slightly. Also, the peak positions (2θ) are shifted at higher values with increasing fluence, which indicates a lattice expansion. XRD pattern shows decrease in crystallinity after irradiation. The amorphous nature of the irradiated samples was confirmed by the absence of some peaks in the XRD pattern.The crystallite size of nanoparticles drastically decreased from 34.68 to 22.66 nm with increasing fluence. The Interplaner distance is almost constant in irradiated nanocomposites. The values of structural parameters are summarized in table 1.

Raman spectra of pristine and irradiated samples are shown in figure 2. The band position of Raman spectra shows significant shift in peak position after irradiation. For spinel ferrites, five characteristic Raman bands $A_{1g} + E_g + 3T_{2g}$are observed in the range of 100 to 800 cm^{-1}. The higher wavenumber in the range of 600-720cm^{-1} are assigned to (M_{tet}-O) vibration at the tetrahedral sites and the lower wavenumber modes in the region of 460-660 cm^{-1} are due to (M_{oct}-O) vibration at the octahedral sites in spinel ferrite [1]. The observed band position are summarized in table 1. In Raman spectra, the region around 1300-1500cm^{-1}is dominated by two bands, which are assigned to anti-symmetric C-N ring stretching and C=C stretching of Ppy [2]. It confirmed the presence of Ppy in pristine and irradiated nanocomposites. The absence of Raman bands in irradiated samples indicates that the octahedral band is more sensitive toward SHI irradiation. The observed shift with increasing irradiation fluence indicates the migration of cations from octahedral sites to tetrahedral sites.

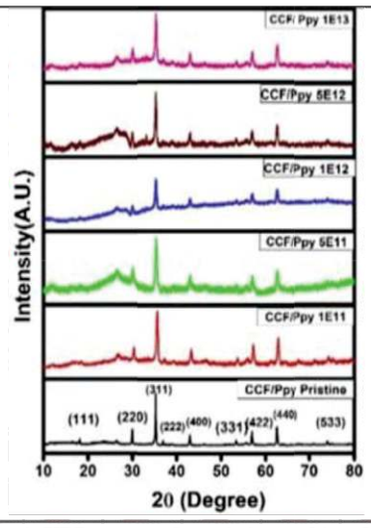

Figure 1: XRD pattern for pristine and irradiated $Co_{0.5}Cu_{0.5}Fe_2O_4$/Ppy nanocomposites

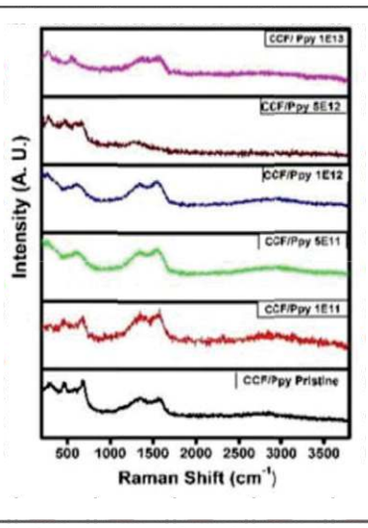

Figure 2: Raman spectra for pristine and irradiated $Co_{0.5}Cu_{0.5}Fe_2O_4$/Ppy nanocomposites

The hysteresis loop of pristine and irradiated $Co_{0.5}Cu_{0.5}Fe_2O_4$/Ppy nanocomposites is shown in figure 3. The saturation magnetization (M_S) and coercivity of pristine sample are 23.75emu.g^{-1} and 1027.29 G respectively. After irradiation M_S decreased from 23.75 to 14.85 emu.g^{-1}. The reduction in M_S with increasing fluence is attributed to the weakening of superexchange interactions and the exchange anisotropy due to spin disorder produced by SHI irradiation [3]. The magnetic parameters of pristine and irradiated $Co_{0.5}Cu_{0.5}Fe_2O_4$/Ppy nanocomposites are tabulated in Table 2. The squareness ratio of SHI irradiated samples is higher than pristine $Co_{0.5}Cu_{0.5}Fe_2O_4$/Ppy nanocomposites. The magnetic materials with high squareness ratio are applicable in storage devices.

Sample	Structural Parameter				Raman shift (cm^{-1})						
	Crystallite Size (nm) ±0.02	Interplaner Distance (Å)	Lat. Parameter (Å)	X-Ray Density (g/cm^3)	T_{2g}	E_g	T_{2g}	T_{2g}	A_{1g}	Anti-symmetric C-N ring stretching	C=C ring stretching
CCF/PPY- Pristine	34.68	5.07	7.74	6.83	218	257	387	-	666	1332	1579
CCF/PPY-1E11	18.94	5.03	7.81	6.65	224	283	381	472	655	1358	1556
CCF/PPY-5E11	16.55	5.06	7.76	6.78	216	-	-	479	661	1332	1541
CCF/PPY-1E12	18.74	5.06	7.79	6.80	221	-	440	453	674	1336	1554
CCF/PPY-5E12	18.79	5.06	7.75	6.80	232	303	459	576	681	1305	-
CCF/PPY-1E13	22.66	5.07	7.79	6.82	221	277	-	-	602	1371	1561

Table 1: Structural parameters and Raman shift for Pristine and irradiated $Co_{0.5}Cu_{0.5}Fe_2O_4$/Ppy nanocomposites

EPR spectra of pristine and irradiated $Co_{0.5}Cu_{0.5}Fe_2O_4$/Ppy nanocomposites are shown in figures 4. The obtained EPR parameters are summarized in table 2. It is observed that the g-values and peak to peak line widths (ΔB_{PP}) decrease after irradiation. Thus after irradiation by 120 MeV Ag ion beam the ΔB_{PP} and thus energy loss is decreased in comparison to pristine.The linewidth is related to the exchange between the spin states, the higher the exchange frequency, the stronger the resonance-line narrowing [4]. This is important for the materials used as transformer cores in the microwave region.

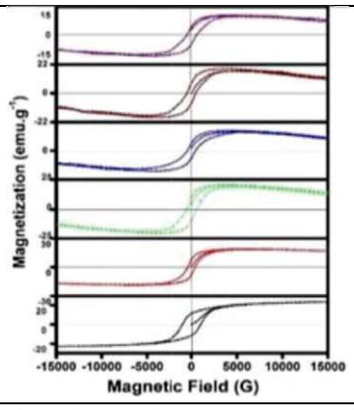

Figure 3: M-H curve for pristine and irradiated $Co_{0.5}Cu_{0.5}Fe_2O_4$/Ppy nanocomposites

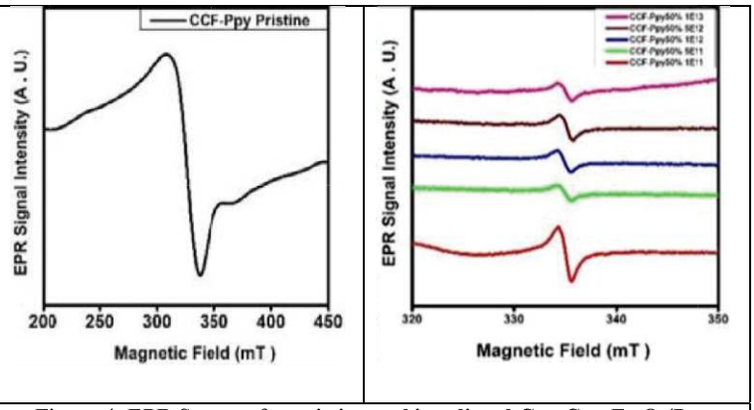

Figure 4: EPR Spectra for pristine and irradiated $Co_{0.5}Cu_{0.5}Fe_2O_4$/Ppy nanocomposites

Table 2. Magnetic and EPR parameters forpristine and irradiated $Co_{0.5}Cu_{0.5}Fe_2O_4$/Ppy nanocomposites

Sample	Magnetic parameters				EPR parameter		
	MS ($emu.g^{-1}$)	Mr ($emu.g^{-1}$)	HC(G)	S (Mr/Ms)	g Value	ΔBPP (mT)	Relaxation Time (picosecond)
CCF/Ppy- Pristine	23.75	10.35	1037.29	0.43	2.061	28.81	1.10
CCF/Ppy-1E11	18.46	11.43	396.04	0.61	1.999	1.306	2.50
CCF/Ppy-5E11	20.33	9.03	500.85	0.44	2.001	1.504	2.17
CCF/Ppy-1E12	18.19	9.16	512.65	0.50	2.003	1.347	2.42
CCF/Ppy-5E12	18.05	8.10	450.75	0.44	2.002	1.310	2.49
CCF/Ppy-1E13	14.85	7.84	427.85	0.52	2.002	1.335	2.44

REFERENCES:

1. A. Subha, M. G. Shalini, B. Sahu, Subasa C. Sahoo .Journal of Materials Science: Materials in Electronics, **29**, no. 24, 20790-20799(2018).
2. Bachhav, S. G., and Patil, D. R. Journal of Materials Science and Chemical Engineering, **3**(10), 30(2015)
3. Almessiere, M. A., Slimani, Y., Trukhanov, A. V., Sadaqat, A., Korkmaz, A. D., Algarou, N. A., and Toprak, M. S. Nano-Structures & Nano-Objects, **26,** 100728(2021).
4. Goryunov, Y. V., and Nateprov, A. N. Physics of the Solid State, **63**(2), 223-231(2021).

5.2.32 Roughening and sputtering kinetics of Pt thin films at different angles of ion irradiation

Munish Kumar [a], Tanuj Kumar [b],*, Ratnesh K. Pandey [c], Sachin Pathak [c], Vandana [d], Ramesh Kumar [a],*

[a]*Department of Physics, Guru Jambheshwar University of Science & Technology, Hisar 125001, Haryana, India*
[b] *Department of Nanosciences & Materials, Central University of Jammu, Jammu 181143, Jammu and Kashmir, India*
[c]*Department of Physics, School of Engineering, University of Petroleum and Energy Studies, Dehradun 248007, Uttarakhand, India*
[d] *Department of Physics, Kurukshetra University, Kurukshetra 136119, India*

Platinum (Pt) thin films of various thicknesses (t_{pt} = 2–6 nm) deposited on Si(100) surface have been investigated for nano structures growth under low energy ion irradiation at different angles of incidence. The resultant surface studies show that angle-dependent sputtering and larger t_{Pt} favor nano structures' formation. Stopping and Range of Ions in Matter (SRIM) simulation, Rutherford back scattering spectrometry (RBS) and kinetic roughening analysis along with scaling components (growth and roughness) predicts that the sputtering and surface diffusion favors surface nanostructuring for thick films at higher angle irradiations. This systematic observation of angle-dependent nanostructuring is important for surface engineering of thin films-based devices.[*for details, see* Materials Letters 303 (2021) 130474]

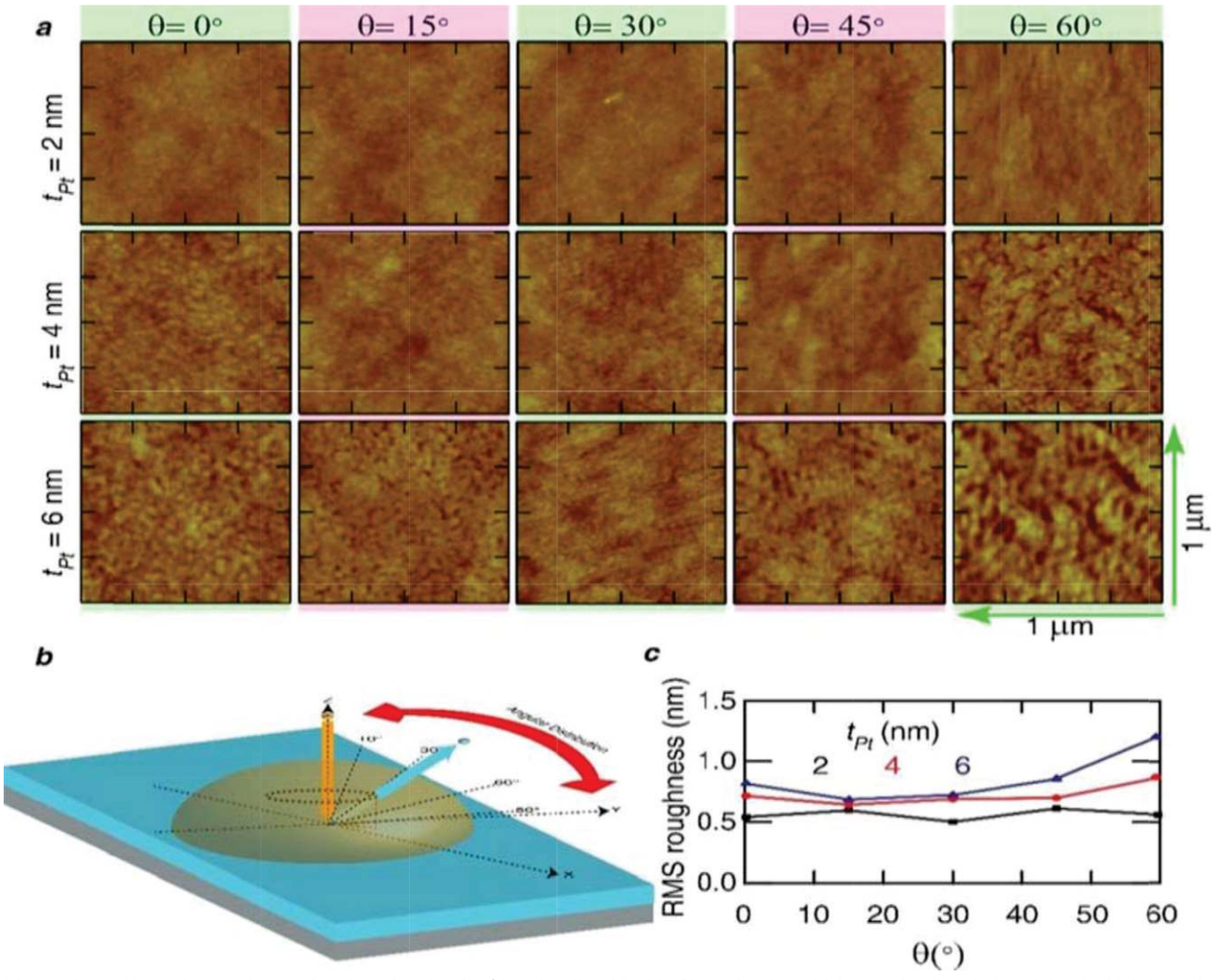

Figure: 2: (a) AFM micrographs as a function of angle of Kr^{+} ions irradiated Pt thin films of various thickness of t_{Pt} (i.e., 2, 4, and 6 nm). (b) Schematic representation of angular incident Kr^{3+} ions, and (c) RMS roughness evaluated from the AFM micrographs as a function of Kr^{+} ions irradiation angle for various t_{pt}.

REFERENCES:

[1] M. Jeyaraj, S. Gurunathan, M. Qasim, M.-H. Kang, J.-H. Kim, A comprehensive review on the synthesis, characterization, and biomedical application of platinum nanoparticles, Nanomaterials (Basel) 9 (2019). https://doi.org/10.3390/ nano9121719.

[2] S. Facsko, T. Dekorsy, C. Koerdt, C. Trappe, H. Kurz, A. Vogt, H.L. Hartnagel, Formation of ordered nanoscale semiconductor dots by ion sputtering, Science **285**, 1551–1553(1999).

5.2.33 Synthesis of bimetallic auag nanoparticles by sequential ion implantation for modifying surface-plasmon-resonance properties

Ksh. Devarani Devi[1,2], Aditya Sharma[1*], Sunil Ojha[2], Jai Parkash1, Ankush Vij[3], Ram K. Sharma[3] and Fouran Singh[2*]

[1]*Department of Physics, Manav Rachna University, Faridabad-124001, Haryana, India.*
[2]*Inter-University Accelerator Centre, Aruna Asaf Ali Marg, New Delhi-110067, India*
[3]*Department of Physics, Centre for Interdisciplinary Research, University of Petroleum and Energy Studies, Dehradun, Uttarakhand 248007, India.*

Surface Plasmon Resonance (SPR) properties of bimetallic nanoparticles have found applications in plasmonic sensors [1-2]. For fabrication of bimetallic $Au_{80}Ag_{20}$ nanoparticles, fused quartz substrates are implanted sequentially at room temperature with 80 keV Au- ions, fluence, 2.4×10^{16} ions/cm^2 and then, 65 keV Ag- ions, fluence, 6×10^{15} ions/cm^2 respectively using negative ion implanter facility, IUAC, New Delhi [3-4]. Pure Au and Ag nanoparticles in quartz matrices are also synthesized with ion fluences, 3×10^{16} ions/cm^2 for reference. The focused ion beams of beam spot size, 6 mm × 6 mm is scanned over the sample area of 15 mm × 15 mm using an electrostatic scanner to obtain uniformity across the sample. A cylindrical shaped tube placed surrounding the ladder is employed as a secondary electron suppressor by applying -400V. The charges striking on the ladder are collected, integrated with a digital current integrator, and counted using a scalar counter to obtain the required ion-fluences. The implanted samples are annealed in air at 600°C, 700°C, 800°C and 900°C for 1 hour. The samples (as implanted and post annealed) are characterized using Rutherford backscattering spectroscopy (RBS), X-ray diffraction (XRD), Transmission electron microscopy (TEM) and absorption spectroscopy.

The formation of crystalline $Au_{80}Ag_{20}$ bimetallic nanoparticles after annealing is confirmed from the X-ray diffraction (XRD) results. The as-implanted $Au_{80}Ag_{20}$ sample shows less intense and broadened diffraction peaks which may be due to the less crystalline nature and small size of $Au_{80}Ag_{20}$ particles. The intensities of the annealed samples at 700 ^{0}C, 900^{0}C are improved with annealing temperature. The two XRD peaks (at ~ 38.4^0 and 44.6^0; from (111) and (200) crystallographic planes of Au, respectively) are evolved after annealing of $Au_{80}Ag_{20}$ sample which indicates the growth of better crystalline nanoparticles. The annealing induced growth of nano particles can be understood by Ostwald ripening. The TEM investigated morphology of 900^{0}C annealed $Au_{80}Ag_{20}$ sample shows implantation of Ag ions close to the depth of pre-existing Au particles and made an alloyed region after annealing. The image also shows few alloys core- Ag shell/satellite nanostructures. There is a diverse distribution of alloyed and spherically shaped nanoparticles. The size is ranging from 2 nm to 20 nm, with most particles of 2–8 nm. RBS spectra convey the diffusion of Au and Ag elements towards the surface after annealing. Ag-related peak (~1700 channel no) is shifted towards higher channel numbers and indicates the mixing of Au and Ag atoms to form an alloyed system after annealing. Some of the tiny Ag particle present in dissolved form in the matrix may not reach the Au NPs to form alloy and they form Ag NPs surrounding the alloy core (satellite nanostructure). The UV–visible absorption studies show intense characteristic SPR peaks of pure Au and pure Ag at 540 nm and 411 nm, respectively which are originated from the resonance of the frequency of the oscillating surface electrons when light fall on them [5-6]. However, for sequentially implanted samples, after Ag implantation, the characteristic SPR peak position of Au has been shifted towards blue (higher energy). The blue shift of the SPR peak may be due to the development of small individual Ag NPs and overlapping of surface electron clouds of Ag with Au NPs. A significant increase in the intensity and red shift in the SPR peak of $Au_{80}Ag_{20}$ nanoparticles are visible as a function of annealing temperature. A minor intensity feature observed between 650 and 700 nm upon increasing the annealing temperature is anticipated that some of the Ag particles may segregate towards the surface (during annealing) and form Ag thin shell, or satellite Ag particles.

REFERENCES:

[1]. A. M. Shrivastav, U. Cvelbar, I. Abdulhalim, Commun. Bio. **4**, 70(2021).
[2]. G. Barbillon, Nanomat**. 10** (2020) 1200.
[3]. X. Meng, T. Shibayama, R. Yu, S. Takayanagi, S. Watanabe, J. Appl. Phys. **114**, 054308-8(2013).
[4]. S. Link, Z. L. Wang, M. A. El-Sayed, J. Phys. Chem. B **103**, 3529(1999).
[5]. P. Slepicka, *et.al.,* Materials **13**, 1(2020).
[6]. K. D. Devi, S. Ojha, F. Singh, Rad. Phy. and Chem. **144,** 141–148(2018).